Horizontal Meandering as a Distinctive Feature of the Stable Boundary Layer

L. MORTARINI,[a,c] D. CAVA,[a] U. GIOSTRA,[b] F. DENARDIN COSTA,[d] G. DEGRAZIA,[c] D. ANFOSSI,[a] AND O. ACEVEDO[c]

[a] *Institute of Atmospheric Sciences and Climate, National Research Council, Bologna, Italy*
[b] *Department of Pure and Applied Sciences (DiSPeA), Università degli Studi di Urbino Carlo Bo, Urbino, Italy*
[c] *Universidade Federal de Santa Maria, Santa Maria, Brazil*
[d] *Universidade Federal do Pampa, Alegrete, Brazil*

(Manuscript received 28 September 2018, in final form 28 June 2019)

ABSTRACT

Oscillations in the horizontal components of the wind velocity associated with oscillations in air temperature during low–wind speed episodes are ubiquitous in the stable boundary layer and are labeled as wind meandering. The meandering structure is recognizable by a clear negative lobe in the Eulerian autocorrelation functions of the horizontal wind velocity components and of the sonic temperature and by a corresponding peak at low frequency in the velocity components and temperature spectra. These distinctive features are used to isolate meandering occurrences and to study its properties in relation to the classical description of the planetary stable boundary layer. It is shown that the ratio of the variance of the wind velocity vertical component over the variance of the composite of the wind velocity horizontal components splits the frequency distribution of meandering and nonmeandering events and divides the nocturnal boundary layer in two different regimes characterized by different turbulent properties. The data comparison with a turbulence model based on Rotta return to isotropy showed that meandering and nonmeandering cases may have similar dynamics. This suggests that meandering may not be connected to a laminarization of the flow and shows that the Rotta scheme may still describe the energetic transfer between wind velocity components in the very stable boundary layer if the Rotta similarity constant c depends on the flux Richardson number. The data confirm a c value of 2.2 for $\mathrm{Ri}_f = 0$ compatible with its conventional value. The analysis presented refers to one year of continuous measurements on 10 levels carried out at a coastal site in southeastern Brazil.

1. Introduction

The characterization of the dynamics of the stable boundary layer (SBL) is complicated by the coexistence of turbulent structures with a variety of submeso phenomena: a mix of nonturbulent, nonstationary processes with scales ranging from the ones of the main turbulent eddies to the one of the smallest mesoscale motions. The relative strength of thermal stratification and shear production determines the switching of the SBL between states where the turbulent structure can be described by the Monin–Obukhov similarity theory and states where nonturbulent oscillatory phenomena dominate the dynamics. Mahrt and Gamage (1987) were the firsts to attempt a division of the SBL in a regime characterized by continuous turbulence and another characterized by intermittent turbulent events. Several studies (e.g., Malhi 1995; Pahlow et al. 2001; van de Wiel et al. 2012a,b) connected the collapse of turbulence to the existence of a maximum sustainable downward heat flux for intermediate stability. If stability increases beyond this limit the heat flux reduces until it is suppressed by the enhanced thermal gradients. Within this picture it seemed natural (Mahrt et al. 1998; Acevedo and Fitzjarrald 2003; Banta et al. 2007; Sorbjan and Grachev 2010) to use the sensible heat flux as a bifurcation parameter to divide the SBL into two regimes: a weakly stable boundary layer where sensible heat flux increases with increasing stability and a very stable regime where the turbulent sensible heat flux is negligible throughout. Following the consideration that wind shear is the primary source of turbulence creation in the SBL and the

Supplemental information related to this paper is available at the Journals Online website: https://doi.org/10.1175/JAS-D-18-0280.s1.

Corresponding author: Luca Mortarini, l.mortarini@isac.cnr.it

DOI: 10.1175/JAS-D-18-0280.1

observation (Vickers and Mahrt 2006) that turbulence never completely disappears, Sun et al. (2012) defined a threshold velocity below which turbulence is generated by local instability and above which it depends on the bulk shear. In other words, as explained by Acevedo et al. (2016) the SBL is vertically connected only when this threshold is exceeded. Through similarity relationships, van de Wiel et al. (2012b) showed that the transition between SBL regimes depends on the wind speed and they suggested a speed limit below which the turbulent heat flux is too weak to balance the radiative cooling. Though identifying different thresholds, all these studies suggest that the wind speed is crucial for defining the dynamics of the SBL.

The study of low–wind speed conditions started for dispersion purposes, noticing that the amplitude of the wind direction variance increases when the wind speed decreases (Joffre and Laurila 1988; Hanna 1990). Later, several studies showed that weak winds are often, if not always, associated with wind meandering, that is, a nonturbulent oscillation of the horizontal wind components (e.g., Sharan et al. 2003; Anfossi et al. 2005; Goulart et al. 2007; Mahrt 2011; Mortarini et al. 2016a). In fact, the meandering phenomenon is ubiquitous in the SBL, Mortarini et al. (2016b) suggested that it may take place when the ratio of the standard deviation of the vertical wind velocity and the standard deviation of the horizontal wind velocity evaluated over 1 h decreases below a threshold. This may relate meandering to a two-dimensionalization of the flow due strong stability, when buoyancy damps the vertical velocity variance, not influencing the horizontal velocity variances that can still have large values. This could suggest a weakening of the pressure redistribution terms linked to the return to isotropy in the wind velocity budget equations. As a matter of fact, it is true that buoyancy will first dampen the vertical velocity variance not affecting the horizontal one. However, when the vertical velocity variance becomes too small, the pressure redistribution should act and route some of the energy from the horizontal velocity variance to the vertical one trying to restore isotropy (Bou-Zeid et al. 2018). This could suggest that the threshold value is related to the return to isotropy, that is, to the maintenance of a Kolmogorov scaling in the vertical velocity and temperature spectra (Katul et al. 2014). Further, Mortarini et al. (2018) noticed that meander may also depend on the wind velocity, with a height-dependent wind speed threshold.

Considering its dependence on a wind threshold, its low turbulence level, and the implicit request that the flow has to be locally decoupled (i.e., detached from the underlying surface due to a lack of significant turbulent transport), it is natural trying to connect the meandering phenomenon to the very stable, weak-wind regime of the SBL described by Mahrt et al. (1998) and Sun et al. (2012).

For this purpose, one year of triaxial sonic anemometry data collected at 10 levels (from 1 to 132 m above the ground) from August 2016 to August 2017 in southeastern Brazil (Acevedo et al. 2018) were analyzed to investigate the properties of the meandering phenomenon and its dependence with height. A technique, which uses the Eulerian autocorrelation functions of the horizontal wind velocities and temperature, developed to identify meandering cases in large datasets (Anfossi et al. 2005; Mortarini et al. 2016b) was used to isolate a large number of meandering cases. The statistics of meandering and nonmeandering data were examined to understand which are the quantities that may identify this behavior and how it is related to a wind speed threshold or stability.

2. Experimental site

The observations analyzed in this paper refer to a measurement campaign carried out from August 2016 to August 2017 at a coastal site in Espirito Santo State (10°31′53″S, 39°48′03″W), southeastern Brazil, in a region where the coastline of the Atlantic Ocean has a south-southwest-to-north-northeast orientation. The continental area in the proximity of the tower is flat for more than 30 km from the site, where the terrain elevation slightly rises to reach 900 m at 150 km. The tower has been deployed at a distance of 245 m from the main buildings of the facilities of Linhares Geração SA, a thermoelectric power plant. Roughness elements near the tower consist of a group of 9-m trees to the east, and the power plant buildings. The turbulent data of wind velocity components u, v, w and sonic temperature θ were continuously collected by three-axis sonic anemometers at 10 Hz in a 140-m tower. The anemometers were model CSAT3B from Campbell Scientific, Inc. The 10-Hz data was recorded at a CR6 datalogger, also from Campbell. Their main axis was oriented facing north, which is roughly the main wind direction and also opposes the power plant buildings. The data were sampled at 11 vertical levels (1, 2, 5, 9, 20, 37, 56, 75, 94, 113, and 132 m), but in the present work the level 20 m was neglected because of instrument malfunction during an appreciable part of the field campaign. The 1- and 132-m anemometers also experienced some instrument malfunctions during the campaign; this explains why the total number of measured hours at those levels is lower (Table 1). Since the focus of this work is the SBL, only nighttime data (from 2200 to 0500 LT) were considered.

TABLE 1. Number of cases for meandering class at each level. In the analysis only meandering and nonmeandering cases were used.

Height (m)	No. of meandering hours	No. of nonmeandering hours	No. of mixed hours	Total No. of hours
132	112	143	261	516
113	325	231	579	1135
94	324	236	504	1064
75	322	266	512	1100
56	295	240	456	991
37	306	237	456	999
9	231	219	601	1051
5	122	255	720	1097
2	116	276	811	1203
1	22	96	201	319

To avoid the influence of hot plumes, data with winds coming from the plant were not considered in the analysis. The exclusion was carried out individually at each measurement height. The wind direction was not the only used criterion for data exclusion; the mean temperature and the temperature variance were considered as well. Hours in which the temperature standard deviation evaluated over 1 min exceeded 4 times the temperature standard deviation evaluated over 1 h and data where the hourly mean temperature was above 50°C were discarded. This explains the slight differences in measurement hours at the height from 2 to 113 m (Table 1). Further information on the experimental site can be found in Acevedo et al. (2018).

3. Data analysis

a. *Identification of meandering*

Since submeso motions can overlap with small-scale turbulence, the choice of a filter time scale is very important in the SBL (Vickers and Mahrt 2006). To capture the range of turbulence scales while excluding spurious contribution from submeso activities, turbulent statistics were evaluated over 1 min. On the other hand, to identify submeso structures it is necessary to choose a filter time scale larger than their typical time scales. Preliminary analyses showed that for the Linhares site the meandering scale is around 35 min; hence, it was chosen to divide the dataset in subsets of 1 h (larger filter time scales will pose problems as well, since they will add contributions from scales larger than submeso). Hence, each hour in the dataset was characterized by 1-h statistics reflecting the low-frequency contribution of submeso motion and (60) 1-min statistics describing the turbulent part of the flow. For each hour the wind velocity components were first rotated into the local streamline reference system by applying a double rotation, then the 1-h and 1-min statistics where evaluated. Linear trends were also removed in the evaluation of the autocorrelation functions. To avoid confusion, in the following σ_i^2 ($i = u, v, w$) refers to the variance of a wind velocity component evaluated over 1 h; $\sigma_{i1\min}^2$ will refer to the variance of a wind velocity component evaluated over 1 min.

Following Mortarini et al. (2016b, 2018) the nonturbulent wavelike oscillations were singled out fitting (see appendix A) the Eulerian autocorrelation functions (EAFs) evaluated from the 1-h subset with the theoretical behavior proposed by Anfossi et al. (2005):

$$R_i(\tau) = e^{-p_i\tau}\cos\left(\frac{2\pi}{T_{*_i}}\tau\right) \quad \text{for} \quad i = u, v, w, \theta, \qquad (1)$$

where p is a parameter connected with the turbulence time scale and T_* is the meandering time scale. When the ratio $m = 2\pi/p_iT_{*i}$ is larger than one the oscillations prevail on turbulence for that quantity, thus all the hours where m is larger than one for u, v, and θ were classified as meandering. On the other hand, the cases where Eq. (1) does not fit the u, v, and θ experimental EAFs were classified as ''nonmeandering.'' An explanation of the fitting procedure can be found in Cava et al. (2019). Clearly, there are ''mixed'' cases where just one or two components oscillate or where Eq. (1) fits the data but with $m < 1$. It was chosen to consider the two extreme behaviors only to better characterize their differences. Since it is not possible to identify meandering from 1-min averages, the 1-min subsets inherit the meandering class from their corresponding hour; that is, if 1 h was classified as meandering, all the 60 min belonging to this hour were classified as meandering. Table 1 shows the number of meandering, nonmeandering, and mixed cases for the Linhares dataset. It is interesting to notice that in the levels between 9 and 113 m the number of meandering cases is larger than the number of nonmeandering cases, while both these numbers are smaller than the mixed cases. Since the mixed cases are likely hours where some kind of nonturbulent activity is present, Table 1 testifies the paramount importance of submeso activity in the SBL. It was quite surprising to find out that, at least for this site, meandering hours are more frequent than hours where the fit was not able to register any activity at all. As it will be shown later in the paper, nonmeandering occurrences prevailed in the earlier portion of the night, while meandering prevailed in the later part of the night, where (see Fig. 8 in Acevedo et al. 2018) the SBL is characterized by the low-wind regime of Sun et al. (2012). Figure 1 shows the vertical profiles of the meandering time scale through the T_* boxplots of for u, v, and θ. As previously observed by

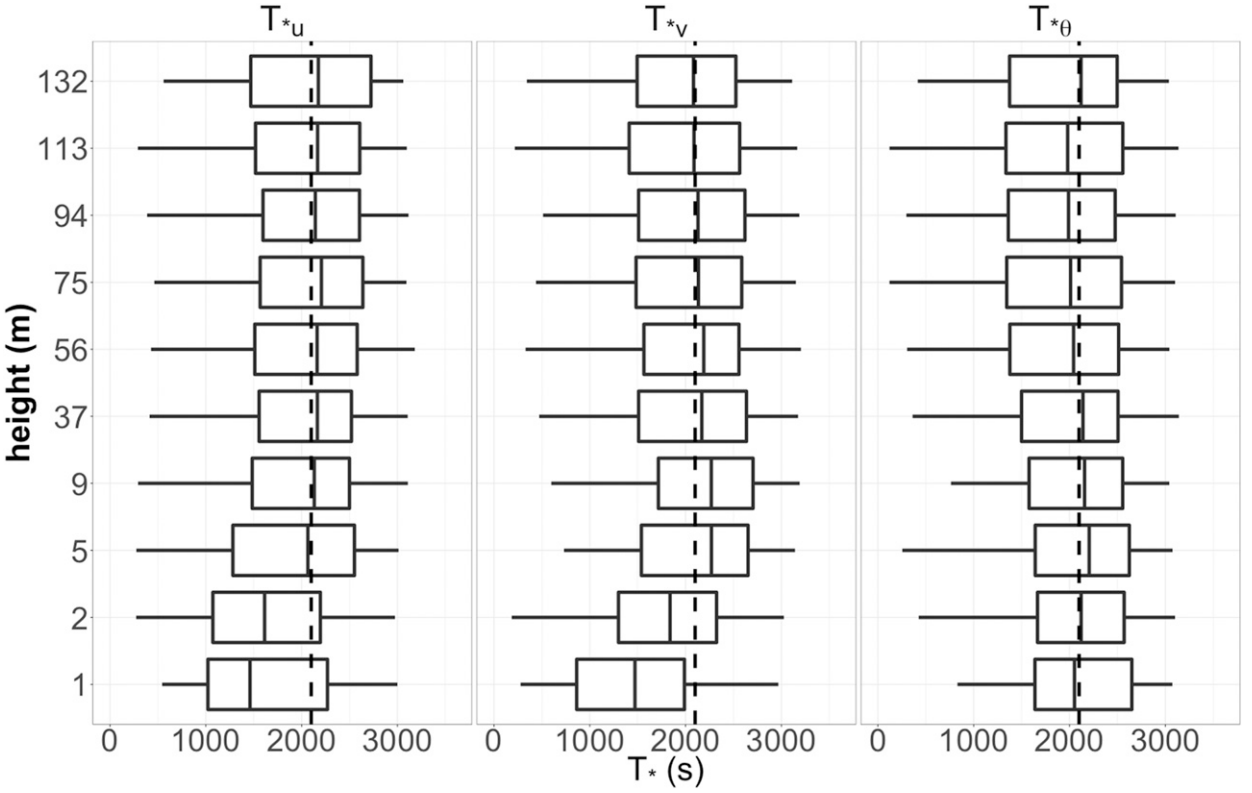

FIG. 1. Meandering time-scale boxplots for the horizontal components u and v of the wind velocity and for the sonic temperature θ. The dashed line refers to a time scale of 2100 s. Data refer to 1-h averages.

Mortarini et al. (2016b) the time scale of temperature oscillation is very similar to those of the horizontal wind velocities components. At 1 and 2 m the oscillation time scales of u and v are smaller. This is probably due to the presence of low vegetation (maximum height ~2 m) in the proximity of the tower. Mortarini et al. (2016b) observed that obstacles could interfere with the meandering motion reducing its amplitude and time scale. As a matter of fact, the temperature does not show a different time scale. The 10 measurement levels allow, for the first time, to see that the meandering phenomenon it is not confined close to the ground. Since above 5 m the median of T_* for the three considered variables at all the heights are close to 2100 s (dashed line in Fig. 1), it might be possible that the meandering time scale is height independent; however, the boxplots may smear out differences for individual cases and thus the physics may get lost.

Cava et al. (2017) and Mortarini et al. (2018) showed that meandering may or may not be associated with internal gravity waves when the vertical velocity component shows an oscillating behavior. Table S1 in the online supplemental material shows the number of meandering hours (Table 1) where the vertical component of the wind velocity oscillates ($m_w > 1$) indicating a possible presence of an internal gravity wave, the number of cases where the fit with Eq. (1) gives $m_w < 1$, that is, cases where there might be submeso activity but without a well-defined oscillation and the number of cases where the fit with Eq. (1) fails. For completeness, the time-scale boxplots of the vertical oscillations, T_{*w}, for cases with $m_w > 1$ at each level are shown in Fig. S1. The number of hours in Table S1 is evidence that w oscillates in a minority of the cases, confirming that meandering does not often depend on the presence of gravity waves and it is not necessarily associated with oscillations of the vertical components of the wind velocity. With the exception of the 9-m level, where the statistics is very limited for the boxplot to be significant, T_{*w} appears to be smaller than the meandering time scales of u, v, and θ (Fig. 1). In the night shown in Cava et al. (2017, their Fig. 2), where meandering was triggered by a clear occurrence of an internal gravity wave, the time scales of u, v, w, and θ showed the same values.

b. *Characterizing the meandering phenomenon*

Once the meandering and nonmeandering hours were detected, it was possible to analyze whether the meandering phenomenon depends on wind speed, stability or on the turbulent kinetic energy. Figure 2a shows the boxplot of the wind speed for meandering and no meandering

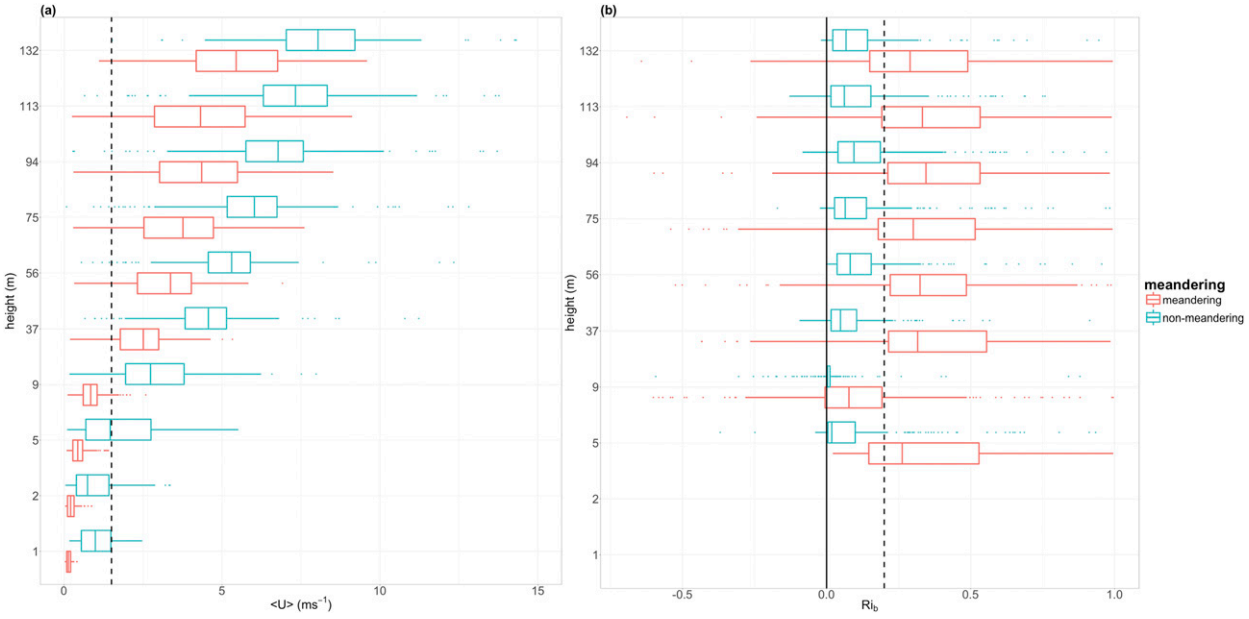

FIG. 2. (a) Boxplots of the mean wind speed at each level; the vertical dashed line refers to 1.5 m s^{-1}. (b) Boxplots of the bulk Richardson number at each level; the vertical dashed line refers to $\mathrm{Ri}_b = 0.2$. Data refer to 1-h averages. Meandering cases are shown in red and nonmeandering cases are in light blue.

cases at each level. It is significant to notice that the interquartile ranges of meandering and nonmeandering cases never cross. However, Fig. 2a also shows that there is not a well-defined wind speed threshold for the meandering occurrence and that the nonturbulent oscillations of the horizontal wind velocity components can occur at higher speeds at higher levels [the vertical dashed line in Fig. 2a refers to the 1.5 m s^{-1} wind speed threshold suggested by Anfossi et al. (2005)]. A good indicator of stability, particularly in light wind conditions, is the bulk Richardson number (Kaimal and Finnigan 1994):

$$\mathrm{Ri}_b = \frac{g}{\theta_p}\frac{\Delta\theta_p \Delta z}{(\Delta\langle U\rangle)^2},$$

where g is the gravitational acceleration, θ_p is the potential temperature, $\Delta\theta_p$ is the difference of the potential temperature measured across a layer of thickness $\Delta z = z - z_0$, z is the height above the ground and z_0 is a reference height, and $\Delta\langle U\rangle$ is the velocity at the height z. The bulk Richardson number was not evaluated for the first two heights. The choice of 2 m (instead of 1 m) as reference height for Ri_b is due to a larger number of available data. For $\mathrm{Ri}_b \ll 0.2$ the flow is in weakly stable conditions and Monin–Obukhov similarity can be applied, while for $\mathrm{Ri}_b > 0.2$ the flow is in very stable conditions and the vertical layers decouple. Figure 2b shows the boxplots of the bulk Richardson number evaluated from 1-h averages at each level; the dashed line refers to $\mathrm{Ri}_b = 0.2$. Even if a threshold value cannot be easily estimated Fig. 2b shows that the meandering phenomenon is more frequent for $\mathrm{Ri}_b > 0.2$ where the mechanical production of turbulence is almost negligible. This value for Ri_b agrees with the classical value attributed to the critical Richardson number as the limit for the laminarization of the flow; the present study evidences that this limit may be more likely associated with the SBL regime transition. The influence of the wind speed on the meandering can be better appreciated in Fig. 3, which shows the histograms evaluated on logarithmically spaced intervals of the wind speed at each level for meandering and nonmeandering cases. The data used in Fig. 3 are averaged over 1 min. If the 1-min average belonged to an hour where meandering was detected, it was plotted in red; otherwise, it was plotted in blue. At all the measurement levels the wind speed displays a bimodal behavior (below 9 m the behavior is trimodal; the secondary peak in the low wind speed part of the nonmeandering histograms might be caused by the roughness elements around the tower; however, the bimodal behavior at the lower measurements heights for nonmeandering cases does not show a dependence on the wind direction). A bimodal behavior was also found for the standard deviation of the velocity components σ_u, σ_v, and σ_w (not shown) and for the dissipation of turbulent kinetic energy ε_u, ε_v, and ε_w (not shown). The bimodality of the frequency distributions of turbulent

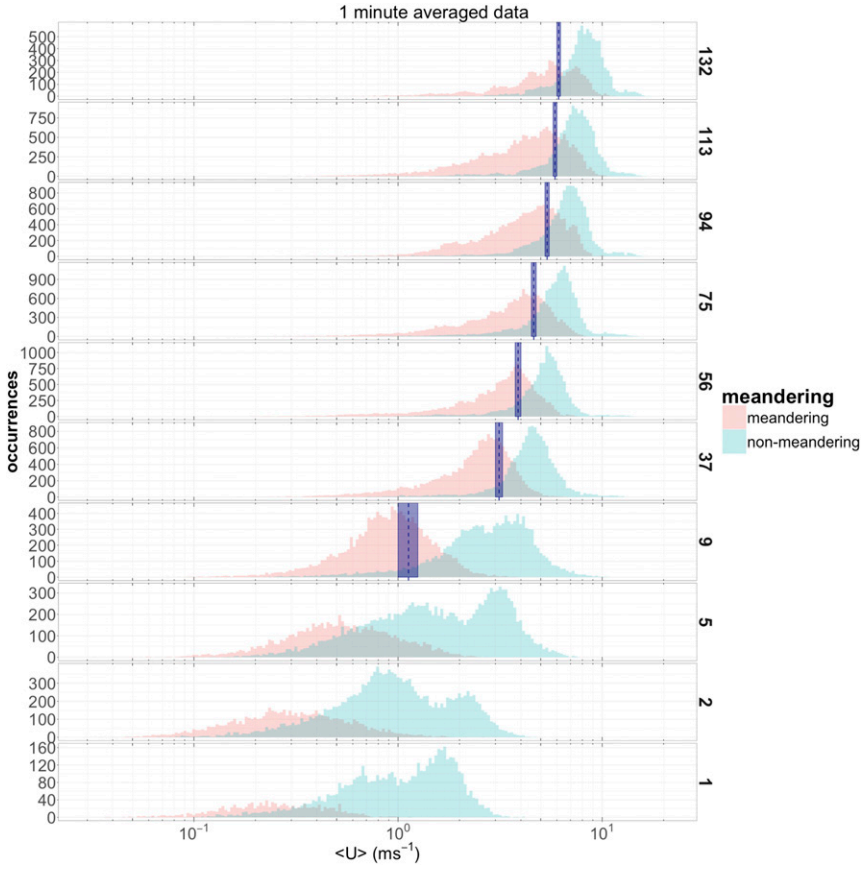

FIG. 3. Wind speed histograms evaluated at each level on logarithmically spaced intervals. Data refer to 1-min averages. Meandering cases are shown in red and nonmeandering cases are in light blue. The dashed lines refer to the U_{HOST} values (Sun et al. 2012) for the Linhares dataset, while the shading refers to the thresholds of $\pm 0.125\ \mathrm{m\,s^{-1}}$.

quantities in stable conditions was observed before (Mahrt et al. 2013; Monahan et al. 2015; Dias-Júnior et al. 2017); Acevedo et al. (2016) associated it to the vertical decoupling of the SBL, but no parameter able to separate the two behaviors was found. In this work, averaging over 1 min not only allowed us to increase the statistics, but it also allowed the comparison with the hockey-stick similarity theory (HOST) of Sun et al. (2012). For each level the wind speed threshold U_{HOST} (Fig. S2) was evaluated and then plotted as a dashed line in Fig. 3 (since it is not a precise evaluation the limits of the wind speed classes used in Fig. S2 were added as shaded areas in Fig. 3). Unfortunately, it was not possible to estimate the thresholds for the first three anemometric levels (5, 2, and 1 m). This was probably due by the presence of low vegetation close to the mast; it is also worth noticing that the U_{HOST} estimated values for the Linhares dataset are lower than those estimated for the CASES-99 dataset (Poulos et al. 2002; Sun et al. 2012). Figure 3 shows that the U_{HOST} values are close to the maxima of the wind speed histograms that refers to meandering hours. This is not surprising because it is reasonable to think that the oscillations of the horizontal wind components take place in a weak turbulent regime when the boundary layer is vertically decoupled. The local decoupling happens when the vertical motions are damped by strong buoyancy; thus, it has to be associated with very low levels of vertical turbulence. At the same time, the presence of meandering suggests that the energy of horizontal motion is large. Mortarini et al. (2016b) observed that the only quantity able to discriminate between meandering and nonmeandering cases is the ratio σ_w/σ_H evaluated for 1-h averaged data. The variances ratio (evaluated over 1 h), σ_w^2/σ_H^2, somehow represents the ratio between the vertical and the horizontal energy associated to the wind: this energy cannot be considered TKE because it contains submeso contributions. Figure 4 shows the frequency distribution evaluated on a logarithmic scale for the σ_w^2/σ_H^2 ratio evaluated

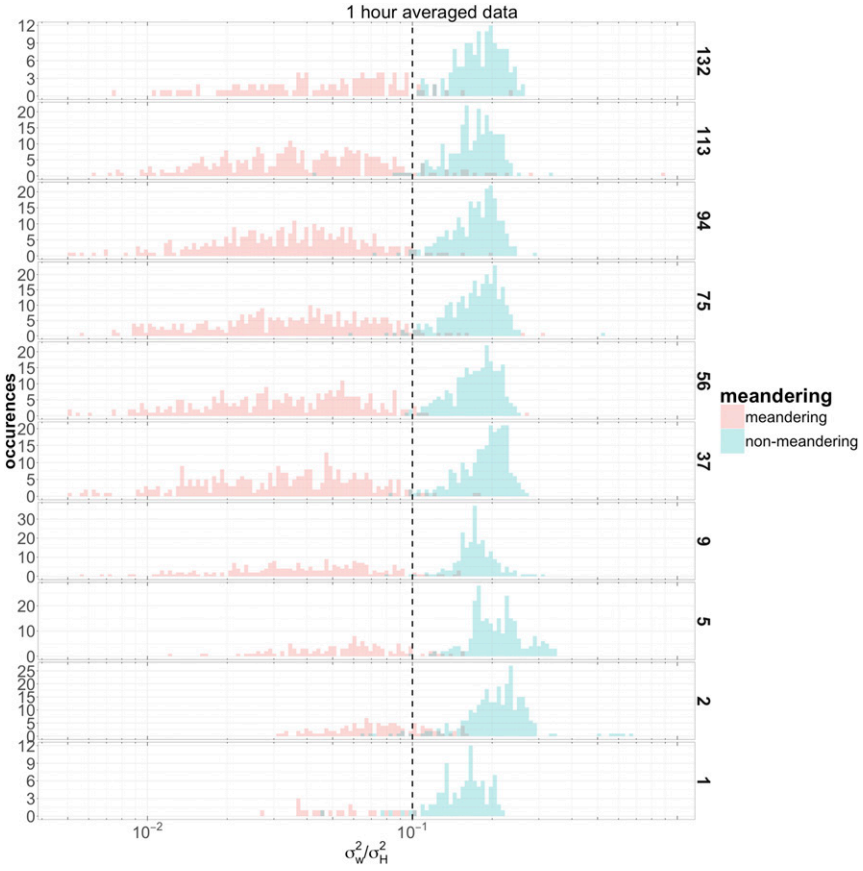

FIG. 4. Frequency distribution of the σ_w^2/σ_H^2 ratio evaluated at each level on logarithmically spaced intervals. Data refer to 1-h averages. Meandering cases are shown in red and nonmeandering cases are in light blue. The dashed line refers to $\sigma_w^2/\sigma_H^2 = 0.1$.

from 1-h averaged data. The separation between the two behaviors is almost striking; at all the measurement levels, it was possible to spot meandering for $\sigma_w^2/\sigma_H^2 < 0.1$. Even if the sharpness of this result is due to having disregarded cases with a mixed behavior (Table 1), the analysis put in evidence that the meandering phenomenon is a characteristic feature of the SBL with a distinctive dynamic. Since the presence of a threshold in the ratio between the vertical and horizontal energy of 1-h subset is a very interesting result its occurrence was checked in two other datasets: Fluxes over Snow Surfaces II (FLOSSII; Mahrt and Vickers 2006) and the Urban Turbulent Project (UTP; Mortarini et al. 2013). Figures S3a and S3b show that indeed a height-independent threshold for σ_w^2/σ_H^2 is able to discriminate the two different behaviors, but that this threshold may be site dependent, even if we do not expect it to be too far from the 0.1 value evaluated in the Linhares dataset. This result is consistent with the two regimes found by Monahan et al. (2015) in the nocturnal boundary layer in Cabauw (the Netherlands): the first regime characterized by low turbulence level, strong stratification, and low wind speeds and the second one characterized by high turbulence level, weak or near-neutral stratification, and high wind speeds. Monahan et al. (2015) also showed that the first regime is associated with lower vertical wind velocity and this is compatible with the low vertical turbulence we found in this work.

Plotting σ_w^2/σ_H^2 as a function of the wind speed helps unfold the role played by the meandering phenomenon in the framework of Sun et al. (2012). Figure 5 shows the dependence of the σ_w^2/σ_H^2 ratio on the mean wind speed for meandering (red points) and nonmeandering (light blue points). To compare its behavior with Sun et al. (2012) the median value (black points and dotted lines) and the boxplot for the same wind speed classes used for Fig. S2 were also plotted and then red vertical dashed lines were added in correspondence to the U_{HOST} values. Figure 5 shows as the σ_w^2/σ_H^2 ratio has two asymptotic behaviors: one for low wind conditions ($\sigma_w^2/\sigma_H^2 = 0.03$) mostly characterized by the presence of

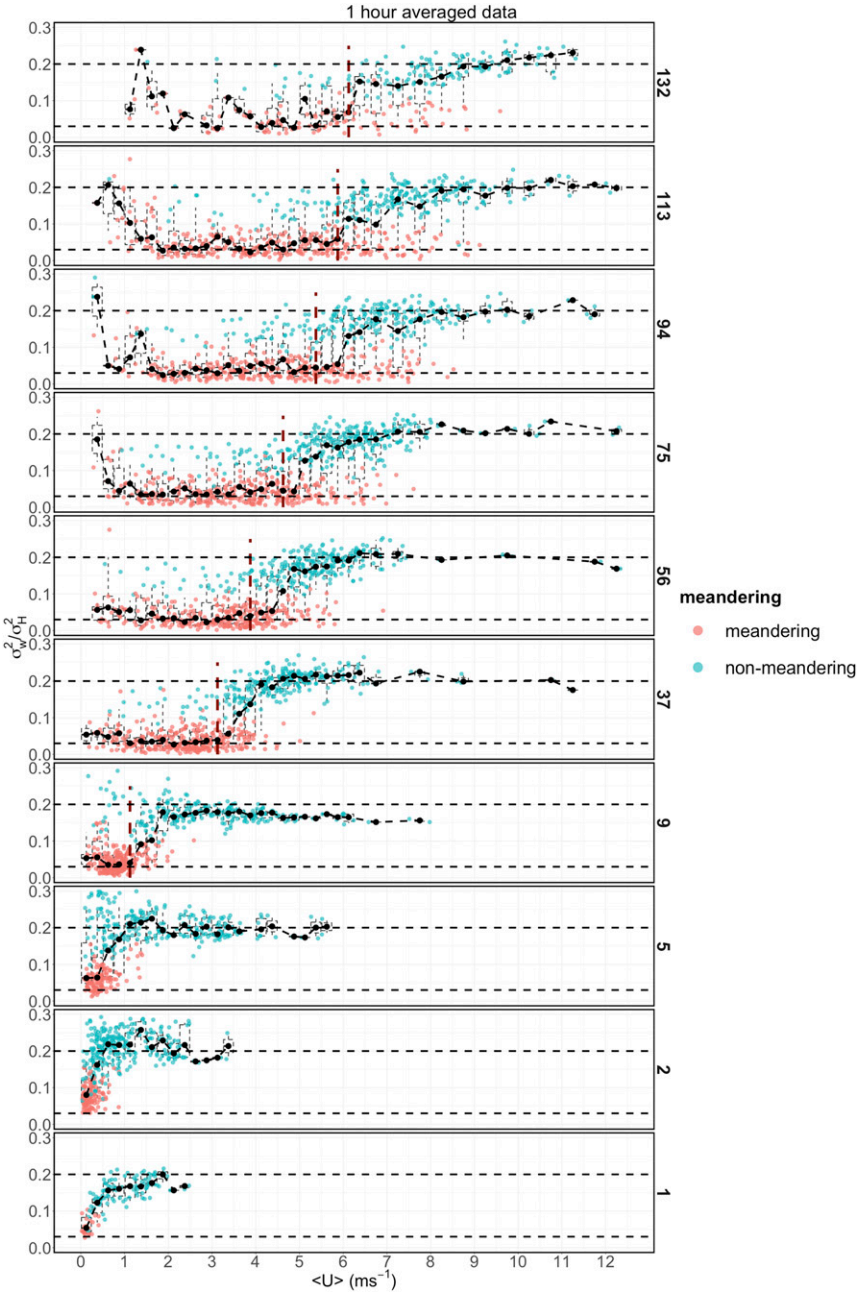

FIG. 5. The σ_w^2/σ_H^2 ratio as a function of the wind speed. Data refer to 1-h averages. Meandering cases are shown in red and nonmeandering cases are in light blue. The dashed horizontal lines refer to $\sigma_w^2/\sigma_H^2 = 0.03$ and $\sigma_w^2/\sigma_H^2 = 0.2$. The red dashed vertical lines refer to the U_{HOST} values (see Fig. S2).

meandering and the other for strong wind conditions ($\sigma_w^2/\sigma_H^2 = 0.20$) mostly characterized by the absence of meandering. The latter asymptotic behavior is known (Luhar et al. 2009; Mahrt 2011; Mahrt et al. 2012). In particular Mahrt (2011) showed that the velocity aspect ratio (i.e., the ratio $\sqrt{2}\sigma_w/\sigma_H$) has an upper limit close to 0.7 (the present value of 0.20 corresponds to a velocity aspect ratio of 0.63). It is very interesting to notice how this value is almost constant with the wind speed at all levels before having an almost abrupt transition when the wind speed is close to U_{HOST}; for $\langle U\rangle < U_{\mathrm{HOST}}$, the average behavior of the data is represented by meandering cases, while for $\langle U\rangle \gtrsim U_{\mathrm{HOST}}$, the average behavior of the data is represented by nonmeandering

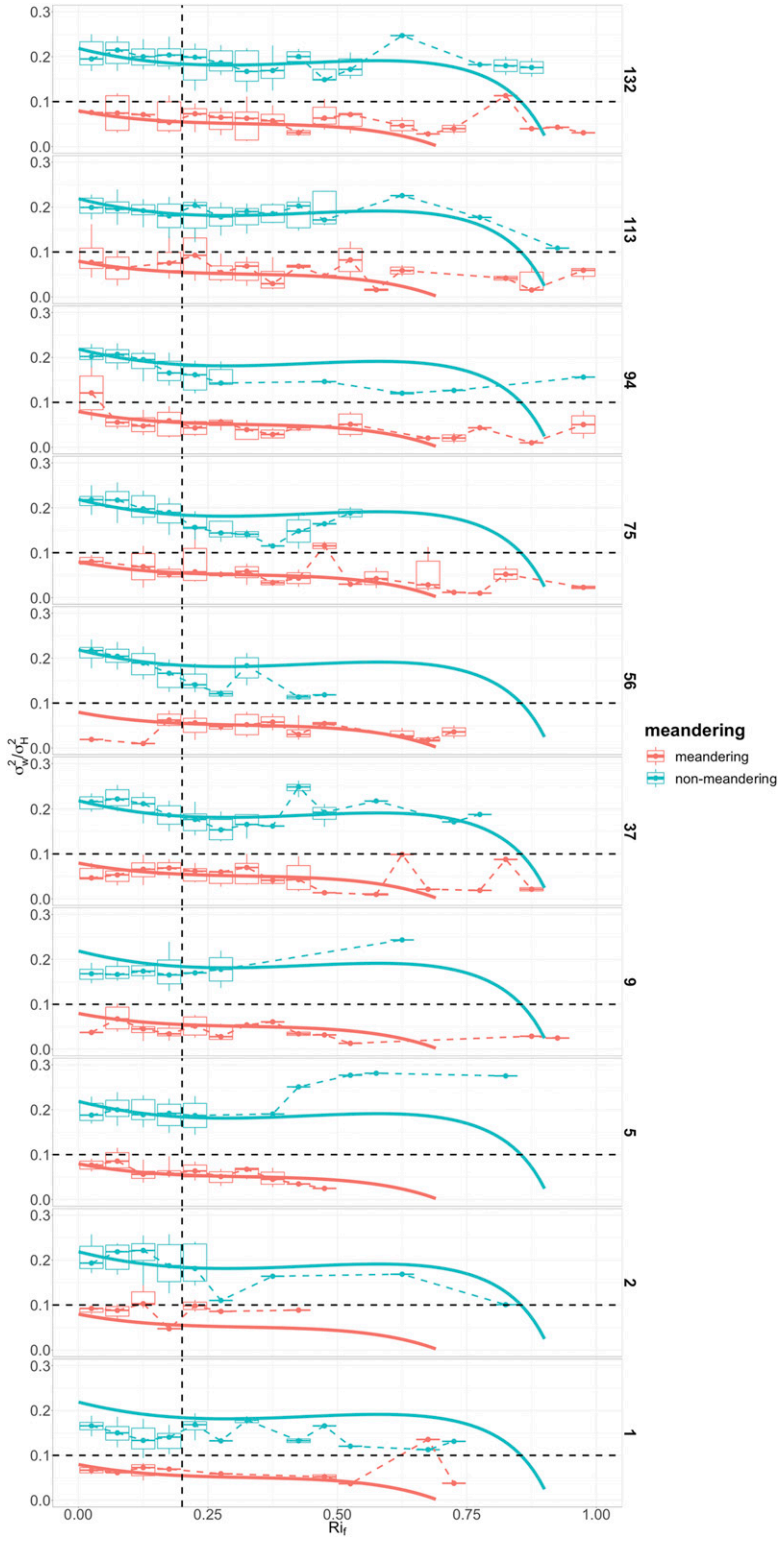

FIG. 6. The σ_w^2/σ_H^2 ratio as a function of the flux Richardson number evaluated at each level. Meandering cases are shown in red and nonmeandering cases are represented in light blue. The vertical dashed lines refer to $Ri_b = 0.2$, while the horizontal dashed line refers to $\sigma_w^2/\sigma_H^2 = 0.1$. The continuous lines are the solutions of Eq. (2), with c evaluated from Eqs. (5).

data. This shows a close link between the σ_w^2/σ_H^2 ratio and U_{HOST} and explains why U_{HOST} does not discriminate between meandering and nonmeandering cases in Fig. 3: low wind speed is a favorable condition for meandering, but it is the partition of TKE between the vertical and horizontal wind components that discriminates between meandering and nonmeandering.

Zilitinkevich et al. (2007) questioned the validity of a stability threshold that separates turbulent and laminar flows. They divided the SBL in two regimes with different characteristics, but both turbulent: one with strong turbulence and another with weak turbulence. A transitional interval of Richardson number separates a regime of fully developed turbulence from a regime of spatially anisotropic and weak turbulence capable of transporting momentum but much less efficient in transporting heat. The small values of σ_w^2/σ_H^2 indeed suggest the presence of a strong spatial anisotropy (Luhar et al. 2009), and Fig. 6, where the dependence of the ratio σ_w^2/σ_H^2 on the flux Richardson number,

$$\mathrm{Ri}_f = \frac{g}{\theta_p}\frac{\langle w'\theta_p'\rangle}{\langle u'w'\rangle dU/dz},$$

is depicted for meandering and nonmeandering cases, seems to agree with Zilitinkevich et al. (2007) that there are two turbulent regimes of different natures, a strong turbulent regime and a weak turbulent regime less efficient in transporting heat. If this is the case it should be expected that the absolute turbulent heat flux presents very low values for the meandering cases. For completeness, mixed meandering cases were added to Figs. 3–5) and are presented in the online supplemental information (Figs. S4–S6). Mixed meandering cases show an intermediate behavior between meandering and nonmeandering cases.

c. Meandering and return to isotropy

Figures 4 and 5 show that, energetically, meandering and nonmeandering cases have distinct behaviors. Considering that meandering cases are typical of higher Richardson numbers, while nonmeandering cases are characterized by lower Richardson number (Fig. 2b); Fig. 6 suggests linking this difference to the anisotropy of the turbulent field for high ($\mathrm{Ri}_f > 0.2$) flux Richardson numbers. Recent studies (Katul et al. 2014; Bou-Zeid et al. 2018) interpret the transitional Richardson number between strong and weak turbulence not in the conventional sense of laminarization but rather in the maintenance by the flow of the Kolmogorov scaling of the wind vertical velocity and temperature. In stable conditions the degree of anisotropy depends on the interplay between the redistribution terms and the (anisotropic) destruction

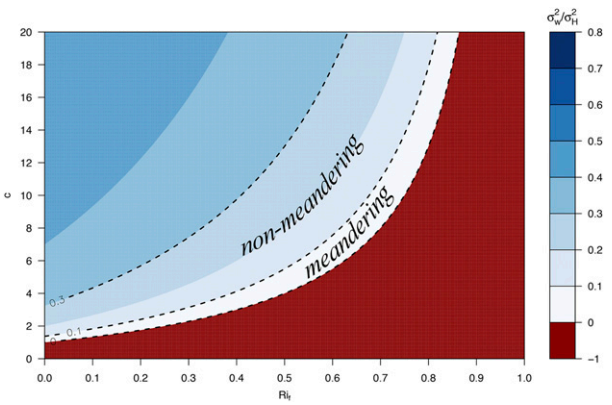

FIG. 7. Filled contours of σ_w^2/σ_H^2 as a function of Ri_f and c [Eq. (2)]. The dashed black lines refer to $\sigma_w^2/\sigma_H^2 = 0$, $\sigma_w^2/\sigma_H^2 = 0.1$, and $\sigma_w^2/\sigma_H^2 = 0.3$. They delimit the σ_w^2/σ_H^2 values for meandering and nonmeandering cases in the Linhares dataset.

by buoyancy (Bou-Zeid et al. 2018). Hence, the small value of the ratio σ_w^2/σ_H^2 cannot be explained only invoking buoyant destruction. It is true that buoyancy will dampen σ_w^2 and σ_H^2 directly. However, the pressure redistribution linked to the return to isotropy will at some point channel some of the energy from the horizontal wind velocity variances to the vertical velocity variance. So, a very small ratio of σ_w^2/σ_H^2 may also require that the return to isotropy become inefficient. To see if this ratio is reflecting the weakening of the redistribution term, we consider the dependence of σ_w^2/σ_H^2 on the flux Richardson number.

In a planar-homogeneous steady flow where the TKE production and dissipation are in equilibrium it is possible to show that (see appendix B)

$$\frac{\sigma_w^2}{\sigma_u^2+\sigma_v^2} = \frac{-\mathrm{Ri}_f + \frac{1}{3}(c-1)(1-\mathrm{Ri}_f)}{1+\frac{2}{3}(c-1)(1-\mathrm{Ri}_f)}, \qquad (2)$$

where c is a parameter connected with a Rotta-type closure for the redistribution terms that expresses the ratio between dissipation and return to isotropy. In stable conditions c must be larger than 1 to prevent σ_w to become negative. While Pope (2000) suggested $c = 1.8$ as a constant optimal value for closure modeling, a constant c value is not able to explain the data behavior depicted in Fig. 6. As stated by Bou-Zeid et al. (2018), $c = 1.8$ will start producing negative value for σ_w for $\mathrm{Ri}_f = 0.21$. Hence, the observed positive σ_w^2/σ_H^2 values beyond $\mathrm{Ri}_f = 0.21$ for both meandering and nonmeandering data shown in Fig. 6 can only be explained by a varying c. To illustrate the reason of such variation, the σ_w^2/σ_H^2 behavior predicted by Eq. (2) is plotted as a function of Ri_f and c in Fig. 7. Figure 6 shows that the σ_w^2/σ_H^2 ratio

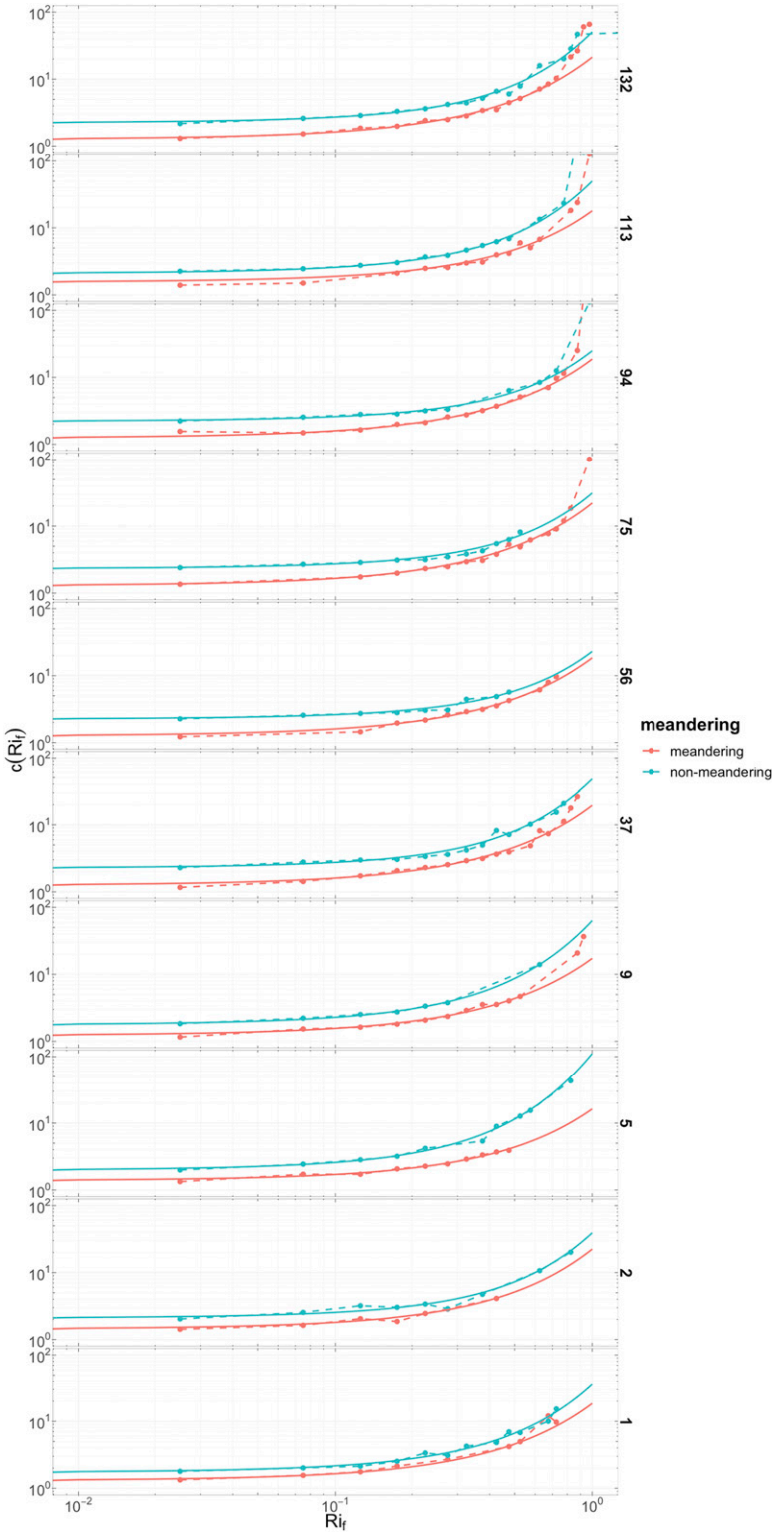

FIG. 8. Parameter c (points and dashed lines) evaluated from data for meandering and nonmeandering cases as a function of the flux Richardson number [Eq. (3)] for the Linhares dataset. The continuous lines refer to a nonlinear fit of the data with the curve $c = a + e^{b\mathrm{Ri}_f}$.

decreases with increasing Ri_f. The dotted lines in Fig. 7 delimit the σ_w^2/σ_H^2 measured values for meandering cases ($0 < \sigma_w^2/\sigma_H^2 < 0.1$) and for nonmeandering cases ($0.1 < \sigma_w^2/\sigma_H^2 < 0.3$) in the Linhares dataset. Figure 7 shows that for data to stay in these ranges, the parameter c necessarily has to increase with stability.

Assuming the validity of Eq. (2), the c dependence on the flux Richardson number can be obtained inverting Eq. (2):

$$c\left(\mathrm{Ri}_f, \frac{\sigma_w^2}{\sigma_H^2}\right) = \frac{1 + \dfrac{\sigma_w^2}{\sigma_H^2} + 2\dfrac{\sigma_w^2}{\sigma_H^2}\mathrm{Ri}_f + 2\mathrm{Ri}_f}{1 - 2\dfrac{\sigma_w^2}{\sigma_H^2} + \dfrac{\sigma_w^2}{\sigma_H^2}\mathrm{Ri}_f - \mathrm{Ri}_f}. \quad (3)$$

Figure 8 shows the median values of c evaluated with Eq. (3) for different Richardson numbers for the Linhares dataset. The values found show an increasing trend that can be fitted by an exponential curve of the kind

$$c(\mathrm{Ri}_f) = a + e^{b\mathrm{Ri}_f}. \quad (4)$$

Performing a nonlinear best fit with Eq. (4) on the c values evaluated at the different heights for meandering and nonmeandering, the continuous lines depicted in Fig. 8 are found. The comparison between the Linhares data and the best fits with Eq. (4) is remarkably good. Equation (4) was preferred to Eq. (3) as an estimator for the c values for its simplicity. The dependence of c on the flux Richardson number seems to imply that as buoyancy increases the redistribution term increases as well to channel energy on the vertical component of the TKE in order to restore isotropy. Table 2 shows the a and b values found by the nonlinear best fit for the different heights of the Linhares data. The exponential fit coefficients a and b do not show a clear dependence on height and they may be assumed constant with height. The median values of the coefficients of Table 2 were chosen as representative for the c behavior at all levels:

$$a = 0.284, \quad b = 2.91 \text{ for meandering cases} \quad \text{and}$$
$$a = 1.165, \quad b = 3.74 \text{ for nonmeandering cases}. \quad (5)$$

It can be noticed that all the values in neutral condition ($\mathrm{Ri}_f = 0$) for the coefficients a and b in Table 2 predict c values within the constraint range $1 < c < 5$ given in Bou-Zeid et al. (2018). Further, the predicted median value of c for nonmeandering cases [Eqs. (5)] in neutral conditions (i.e., $c \approx 2.2$) is close to the value suggested by Pope (2000). On the other hand, the lower value ($c \approx 1.3$) identified in meandering cases is not connected with a relaminarization of the flow. The vertical velocity standard deviation remains finite, while the horizontal velocity components standard deviations increase and can reduce the c parameter to values close to unity.

TABLE 2. Coefficients of the nonlinear best fit performed on the c parameter for the different levels and for meandering and nonmeandering cases for the Linhares dataset.

	$c(\mathrm{Ri}_f) = a + e^{b\mathrm{Ri}_f}$			
	Nonmeandering		Meandering	
Level (m)	a	b	a	b
1	0.736	3.55	0.310	2.90
2	1.110	3.64	0.447	3.09
5	0.984	4.70	0.390	2.77
9	0.771	4.14	0.234	2.84
37	1.280	3.84	0.259	2.96
56	1.260	3.08	0.268	2.90
75	1.330	3.40	0.298	4.08
94	1.220	3.17	0.252	2.92
113	1.100	3.89	0.557	2.86
132	1.240	3.90	0.270	3.05

Finally, it is possible to substitute Eq. (4) evaluated with the coefficients a and b presented in Eqs. (5) into Eq. (2) and compare the σ_w^2/σ_H^2 predictions of the model with the Linhares data. The continuous lines in Fig. 6 represent the model predictions at the various heights. Figure 6 shows that, assuming for the scale-ratio parameter c an exponential dependency on Ri_f, a Mellor and Yamada (1982) model with a Rotta-type closure is able to explain the σ_w^2/σ_H^2 behavior up to very stable Richardson numbers (using the model with a constant value for the ratio of dissipation and the redistribution term leads to a poor comparison with the data; not shown). The comparison with the model [Eq. (2)] may also evidence a similar dynamic of meandering and nonmeandering cases. Since the turbulent kinetic energy dissipation rate is isotropic and finite (Fig. S7) and since it seems that a ''Rotta''-like model applies for shuttling energy back and forth between the horizontal velocity components and the vertical velocity component, the meandering phenomenon might not be related to laminarization but it could be considered, at least at the level of second-order statistics and energetics, as an approximation of 2D planar turbulence (but still with a finite σ_w and ε_w). The analysis was repeated for the FLOSSII dataset. The results are shown in Figs. S8 and S9 and in Table S2, and they are in very good agreement with the ones obtained for the Linhares tower.

d. The role of the turbulent heat flux in the meandering phenomenon

Figure 9 depicts the turbulent heat flux $H = \rho C_p \langle w'\theta' \rangle$, where ρ is the air density and C_p is the specific heat at

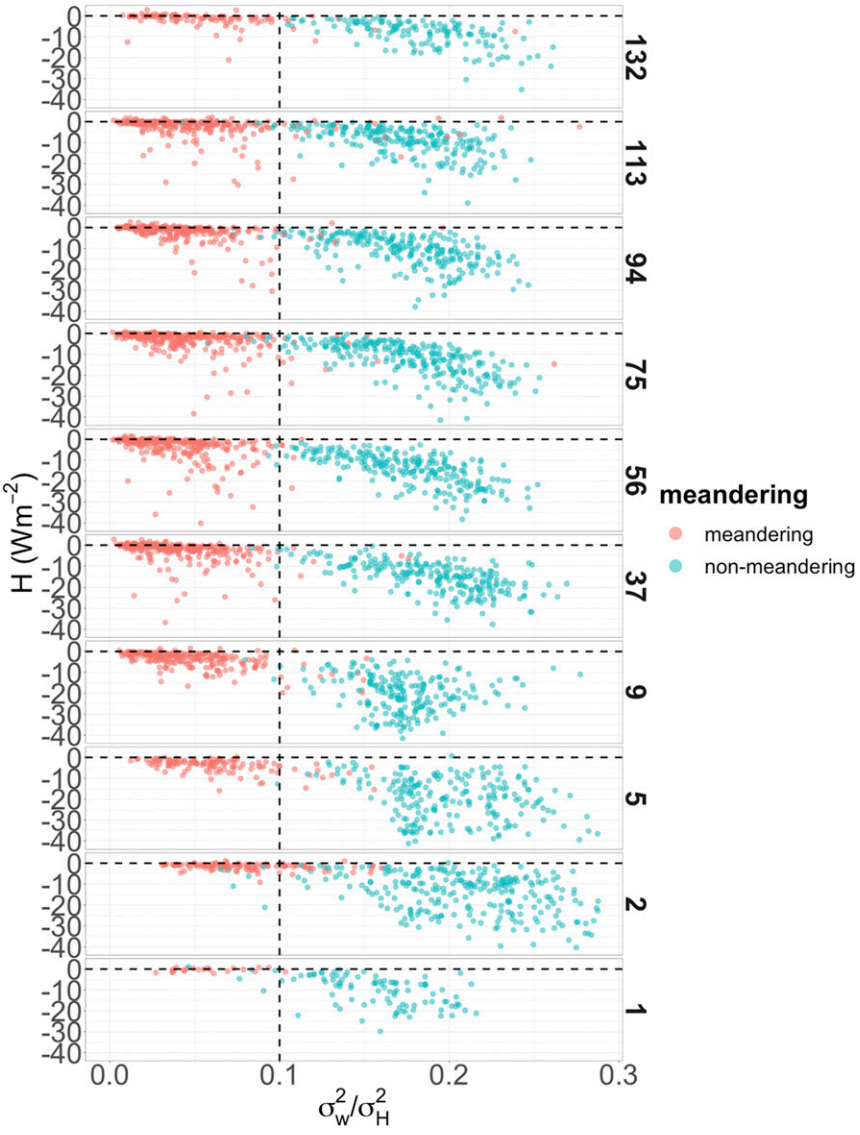

FIG. 9. Absolute turbulent heat flux as a function of the ratio between the vertical and the horizontal energy of the flow. Meandering cases are shown in red and nonmeandering are in light blue. The dashed line refers to $\sigma_w^2/\sigma_H^2 = 0.1$.

constant pressure as a function of σ_w^2/σ_H^2. In this picture the variances of the wind velocity components are evaluated averaging over 1 h, while the turbulent heat flux is evaluated over 1 min and then averaged over 1 h. Not surprisingly meandering cases show extremely low values of H, confirming that the vertical turbulence is too weak to sustain a turbulence heat flux able to balance the radiative cooling (van de Wiel et al. 2012a). The dependence of the absolute turbulent heat flux on the bulk Richardson number evaluated at 37 m is shown in Fig. 10. Meandering cases are put in evidence by red contours, while nonmeandering cases are put in evidence by blue contours. In accordance with Baas et al. (2018), a clear absolute heat flux maximum for $0.01 < \mathrm{Ri}_{b37\mathrm{m}} < 0.02$ is found. This maximum may be interpreted as a threshold between weakly stable and very stable boundary layer regimes. As a matter of fact, meandering cases are all found for values of the bulk Richardson number larger than this maximum. Further, if Fig. 10 is compared with Fig. 6 of Baas et al. (2018), it can be seen that the majority of the present cases occupying the bottom-right part of the plot, where in Baas et al. (2018) figure there is a slight difference of occurrences between measured and modeled data, are meandering cases. This may confirm the difficulty of models in reproducing the meandering phenomenon. The poor model performance for

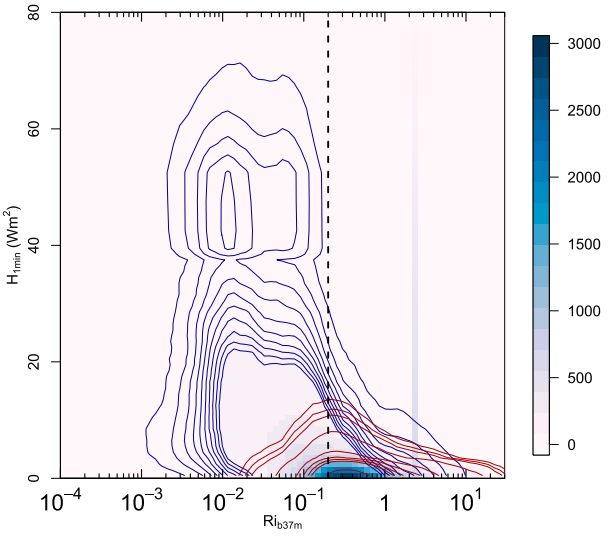

FIG. 10. Relation between the absolute turbulent heat flux and the Bulk Richardson number evaluated at 37 m Ri_{b37m}. Colors indicate the number of occurrences for the all dataset; the red contours refer to meandering data, and the blue contours to nonmeandering data. The dashed vertical line corresponds to $Ri_{b37m} = 0.2$.

meandering cases may be connected with the c values [Table 2 and Eqs. (5)] encountered in section 3d. The $c \approx 1.3$ in neutral condition is well below the prescribed value of $c = 1.8$. Figure 11 shows the dependence of the turbulent heat flux evaluated on 1-min averages on the hour of the night for meandering and nonmeandering data. The number over each boxplot refers to the number of hours considered. It is interesting to see how the turbulent heat flux medians (the dashed lines in Fig. 11) for nonmeandering cases exhibit a behavior in agreement with a progressive increase of the atmospheric stability in the nocturnal stable boundary layer; that is, the absolute heat flux shows a maximum value around 2200 LT and then decreases while the boundary layer stability increases. The transitional behavior from a weak stability in the first half of the night to a strong stability after midnight has been already described for the same experimental site (see Fig. 7 in Acevedo et al. 2018). The progressively decreasing of the heat flux (in absolute value) is consistent with a progressively suppression of turbulent mixing unable to balance the radiative cooling when that stability increases (Lan et al. 2018). On the contrary, meandering case medians do not show a time evolution for the turbulent heat flux. Further, it can be noticed how the number of meandering cases increases during the night, while the number of nonmeandering cases simultaneously decreases, confirming that only in the very stable boundary layer the conditions necessary to produce the horizontal oscillations of the wind vector are encountered.

4. Conclusions

One year of anemometric data sampled at 10 levels were analyzed to study the oscillations of the horizontal wind velocity components and the air temperature in the stable boundary layer. Using the Eulerian autocorrelation functions to discriminate between data with a strong oscillating signature (oscillations on u, v, and θ) and data with no hint of oscillations allowed us to present some original features of the meandering phenomenon. While nonmeandering cases can be associated with low values of the bulk Richardson number, larger wind speeds, and larger negative values of the turbulent heat flux, meandering cases can be associated with low wind speeds, almost negligible turbulent heat fluxes, and large values of the bulk Richardson number. As a matter of fact, we may claim that nonmeandering cases are typical of the weakly stable boundary layer, while meandering cases are typical of the very stable boundary layer. The horizontal wind oscillations only dominate the flow dynamics when buoyancy inhibits vertical motions and the boundary layer becomes vertically decoupled. A threshold in the ratio of the variance of the vertical wind velocity component and the variance of the horizontal wind velocity component is able to discriminate between meandering and nonmeandering motions. The value of the σ_w^2/σ_H^2 threshold does not depend on the measurement height, but it seems to be site dependent. Nevertheless, the transition between the meandering and nonmeandering behavior is determined by the wind speed threshold defined by the hockey-stick similarity theory. The dependence of the σ_w^2/σ_H^2 ratio on the flux Richardson number showed that meandering might be considered as an ''approximation'' of highly anisotropic turbulence (with a finite σ_w and ε_w), and hence, it may not be related with flow laminarization. A notable side result of the analysis presented in this paper is that the Rotta constant c that describes the ratio of dissipation and the redistribution terms in the velocity variance budget equations might vary with Ri_f and could be included in Mellor and Yamada (1982) models after the present result is confirmed by other experiments in the very stable boundary layer, while the Rotta scheme with a constant c used by Mellor and Yamada (1982) remains a cornerstone closure in numerical weather forecast models.

Noteworthy, meandering was encountered at all the measurements level and, with the exception of the levels closer to the ground, the median values of the oscillation time scales of the streamwise velocity, the cross-stream

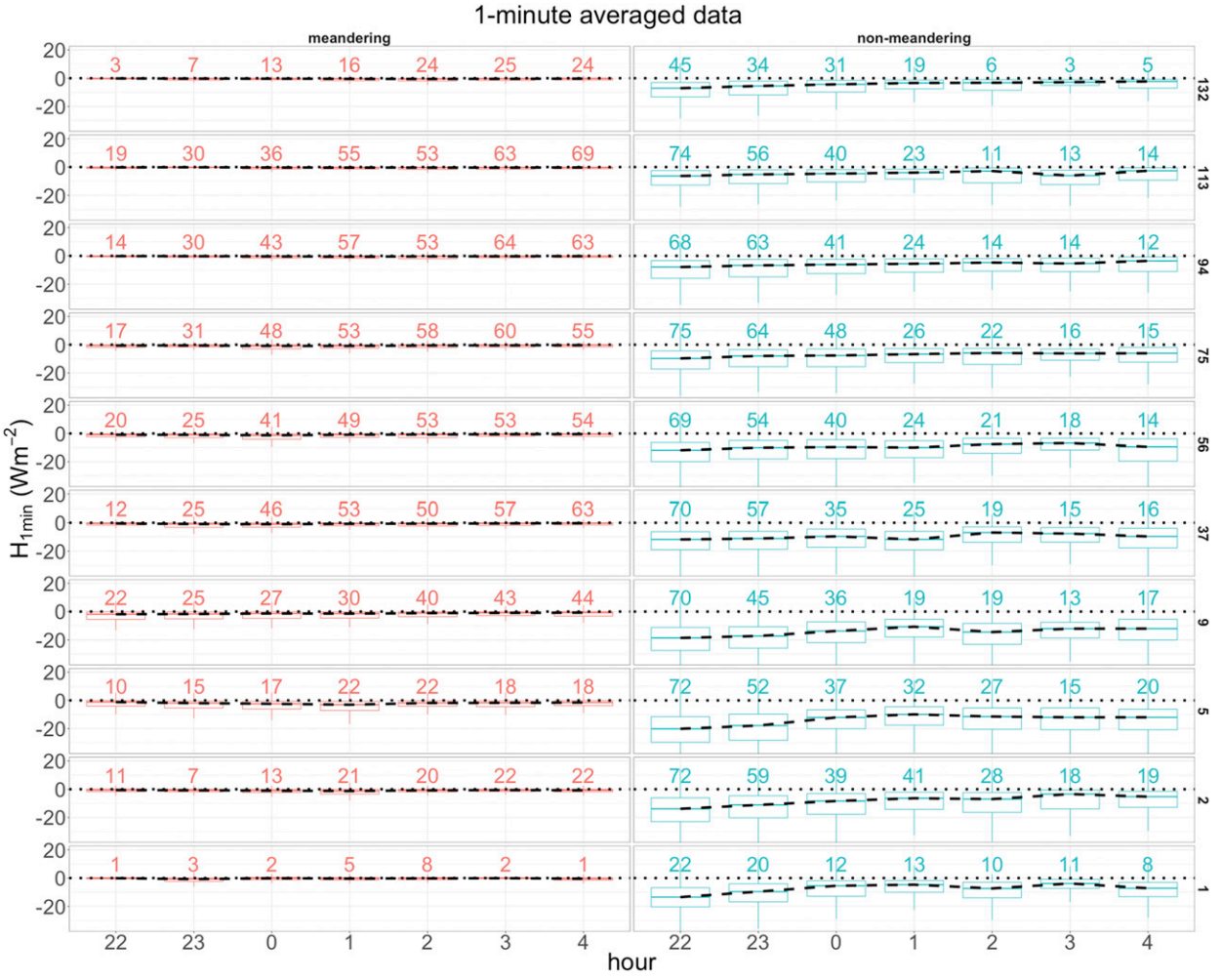

FIG. 11. Boxplots of the absolute turbulent heat flux evaluated at each level from 1-min averages; the number over each box refers to the number of hours considered. (left) Meandering cases are shown in red and (right) nonmeandering are in light blue. The black dashed line connects the median point of the boxplot and the dotted lines refer to null absolute heat flux.

velocity, and the wind temperature show similar, height-independent values.

Acknowledgments. The authors are grateful to one of the anonymous reviewers for the suggestion of exploring the link between $\sigma_w^2/(\sigma_u^2 + \sigma_v^2)$ and the flux Richardson number. The study was developed within the context of a research and development project sponsored by the companies Linhares Geração S.A. and Termelétrica Viana S.A. (APLPED6932_ PROJETOPED_0114), and named ''Desenvolvimento de um modelo operacional para simulação em tempo real da dispersão atmosférica de poluentes emitidos por termelétrica a gás natural.'' The project is within the context of the investment program in research and development, regulated by the Brazilian National Agency for Electric Energy. The authors are deeply thankful for all of the support provided by these companies for the development of the present work. Finally, the authors acknowledge the collaboration with the Marche Region (Italy), and in particular the ''Environmental assessments and authorizations, air quality and natural protection'' section.

APPENDIX A

Fitting the Autocorrelation Function with Eq. (1)

The fitting procedure is based on the nls function of the R software (R Core Team 2017; Bates and Chambers 1992), which determines the nonlinear least squares estimates of the parameters of a nonlinear model. The nls function provides an estimate (first guess) of the p and q parameters together with their standard error. The algorithm depends on the choice of the starting estimates

of the p and q parameters. During the analysis the p and q parameters are evaluated performing the fit with 30 different couples of starting estimates from two uniform distributions [in the ranges of $(10^{-5}\,s^{-1}, 10^{-3}\,s^{-1})$ for p and $(10^{-6}\,s^{-1}, 10^{-3}\,s^{-1})$ for q] and then choosing the couple that minimizes the residual standard deviation. The fit to Eq. (1) fails if the fitting algorithm fails for all the starting couples. It can be verified that either the fit fails for all the 30 couples or it succeeds for the majority of them (more than for the 80% of the couples) providing identical values for the p and q parameters, that is, showing no dependence on the first guesses.

APPENDIX B

Turbulence Model

To evaluate Eq. (2) an idealized SBL is considered where the focus is on a stationary and planar homogeneous flow at high Reynolds number in the absence of subsidence. All transport terms, including turbulent transport and pressure transport, are neglected. Applying these assumptions to the three velocity variance budgets yields (Stull 1988)

$$\begin{aligned}\sigma_u^2:&\quad 0 = P_m + R_u - \epsilon_u,\\ \sigma_v^2:&\quad 0 = R_v - \epsilon_v,\\ \sigma_w^2:&\quad 0 = B + R_w - \epsilon_w,\end{aligned} \tag{B1}$$

where R_u, R_v, and R_w are the energy redistribution terms for u, v, and w, respectively; P_m is the mechanical production; and B is the buoyant production/destruction [$P_m = -\langle u'w'\rangle dU/dz$; $B = (g/\theta_p)\langle w'\theta'_p\rangle$].

It can also be assumed an isotropic small-scale dissipation ε that remains finite (i.e., the flow must remain turbulent and no laminarization occurs) so that

$$\epsilon_u = \epsilon_v = \epsilon_w = \frac{1}{3}\varepsilon, \quad \text{where} \quad \varepsilon = P_m + B = P_m(1 - \mathrm{Ri}_f).$$

Further, the energy redistribution terms can be written using a Rotta-type closure (Mellor and Yamada 1982) type:

$$\begin{aligned}R_u &= -\frac{q}{\lambda_1}\left(\sigma_u^2 - \frac{q^2}{3}\right),\\ R_v &= -\frac{q}{\lambda_1}\left(\sigma_v^2 - \frac{q^2}{3}\right),\\ R_w &= -\frac{q}{\lambda_1}\left(\sigma_w^2 - \frac{q^2}{3}\right),\end{aligned} \tag{B2}$$

where $q^2 = \sigma_u^2 + \sigma_v^2 + \sigma_w^2$ and $\epsilon = q^3/\lambda_2$. The λ_1 and λ_2 are two length scales that are both proportional to a length scale l_m, but these proportionality constants differ. That is, $\lambda_1 = b_1 l_m$ and $\lambda_2 = b_2 l_m$. The b_1 and b_2 coefficients depend on the choice of l_m, but this will not affect the conclusions. Inserting Eq. (B2) in the variance budgets [Eq. (B1)], it can be readily shown that

$$\begin{aligned}\sigma_u^2:&\quad 0 = P_m - \frac{q}{\lambda_1}\left(\sigma_u^2 - \frac{q^2}{3}\right) - \frac{1}{3}\varepsilon,\\ \sigma_v^2:&\quad 0 = -\frac{q}{\lambda_1}\left(\sigma_v^2 - \frac{q^2}{3}\right) - \frac{1}{3}\varepsilon,\\ \sigma_w^2:&\quad 0 = B - \frac{q}{\lambda_1}\left(\sigma_w^2 - \frac{q^2}{3}\right) - \frac{1}{3}\varepsilon.\end{aligned} \tag{B3}$$

Now, assuming that $\lambda_2/\lambda_1 = c$, it is easy to show that

$$\frac{\sigma_w^2}{\sigma_u^2 + \sigma_v^2} = \frac{-\mathrm{Ri}_f + \frac{1}{3}(c-1)(1-\mathrm{Ri}_f)}{1 + \frac{2}{3}(c-1)(1-\mathrm{Ri}_f)}. \tag{B4}$$

Equation (B4) shows how the ratio $\sigma_w^2/(\sigma_u^2 + \sigma_v^2)$ depends on the flux Richardson number and on c. The parameter c is independent from the choice of the length scale l_m. However, c is expected to depend on stability. The c describes the ratio of the dissipation on the redistribution term. Since, with increasing stability the return to isotropy becomes less efficient relative to dissipation, λ_1 is expected to decrease while λ_2 remains constant.

REFERENCES

Acevedo, O. C., and D. R. Fitzjarrald, 2003: In the core of the night—Effects of intermittent mixing on a horizontally heterogeneous surface. *Bound.-Layer Meteor.*, **106**, 1–33, https://doi.org/10.1023/A:1020824109575.

——, L. Mahrt, F. S. Puhales, F. D. Costa, L. E. Medeiros, and G. A. Degrazia, 2016: Contrasting structures between the decoupled and coupled states of the stable boundary layer. *Quart. J. Roy. Meteor. Soc.*, **142**, 693–702, https://doi.org/10.1002/qj.2693.

——, and Coauthors, 2018: Monitoring the micrometeorology of a coastal site next to a thermal power plant from the surface to 140 m. *Bull. Amer. Meteor. Soc.*, **99**, 725–738, https://doi.org/10.1175/BAMS-D-17-0134.

Anfossi, D., D. Oettl, G. Degrazia, and A. Goulart, 2005: An analysis of sonic anemometer observations in low wind speed conditions. *Bound.-Layer Meteor.*, **114**, 179–203, https://doi.org/10.1007/s10546-004-1984-4.

Baas, P., B. J. H. van de Weil, S. J. A. van der Linden, and F. C. Bosveld, 2018: From near-neutral to strongly stratified: Adequately modelling the clear-sky nocturnal boundary layer at Cabauw. *Bound.-Layer Meteor.*, **166**, 217–238, https://doi.org/10.1007/s10546-017-0304-8.

Banta, R. M., L. Mahrt, D. Vickers, J. Sun, B. B. Balsley, Y. L. Pichugina, and E. J. Williams, 2007: The very stable boundary

layer on nights with weak low-level jets. *J. Atmos. Sci.*, **64**, 3068–3090, https://doi.org/10.1175/JAS4002.1.

Bates, D. M., and J. M. Chambers, 1992. Nonlinear models. *Statistical Models in S*, J. M. Chambers and T. J. Hastie, Eds., Wadsworth and Brooks/Cole, 421–454.

Bou-Zeid, E., X. Gao, C. Ansorge, and G. G. Katul, 2018: On the role of return to isotropy in wall-bounded turbulent flows with buoyancy. *J. Fluid Mech.*, **856**, 61–78, https://doi.org/10.1017/jfm.2018.693.

Cava, D., L. Mortarini, U. Giostra, R. Richiardone, and D. Anfossi, 2017: A wavelet analysis of low-wind-speed submeso motions in a nocturnal boundary layer. *Quart. J. Roy. Meteor. Soc.*, **143**, 661–669, https://doi.org/10.1002/qj.2954.

——, ——, D. Anfossi, and U. Giostra, 2019: Interaction of submeso motions in the Antarctic stable boundary layer. *Bound.-Layer Meteor.*, https://doi.org/10.1007/s10546-019-00426-7

Dias-Júnior, C. Q., L. D. A. Sá, E. P. Marques Filho, R. A. Santana, M. Mauder, and A. O. Manzi, 2017: Turbulence regimes in the stable boundary layer above and within the Amazon forest. *Agric. For. Meteor.*, **233**, 122–132, https://doi.org/10.1016/j.agrformet.2016.11.001.

Goulart, A., G. Degrazia, O. Acevedo, and D. Anfossi, 2007: Theoretical considerations of meandering wind in simplified conditions. *Bound.-Layer Meteor.*, **125**, 279–287, https://doi.org/10.1007/s10546-007-9179-4.

Hanna, S. R., 1990: Lateral dispersion in light-wind stable conditions. *Nuovo Cimento*, **13C**, 889–894, https://doi.org/10.1007/BF02514777.

Joffre, S. M., and T. Laurila, 1988: Standard deviations of wind speed and direction from observations over a smooth surface. *J. Appl. Meteor.*, **27**, 550–561, https://doi.org/10.1175/1520-0450(1988)027<0550:SDOWSA>2.0.CO;2.

Kaimal, J. C., and J. J. Finnigan, 1994: *Atmospheric Boundary Layer Flows*. Oxford University Press, 289 pp.

Katul, G. G., A. Porporato, S. Shah, and E. Bou-Zeid, 2014: Two phenomenological constants explain similarity laws in stably stratified turbulence. *Phys. Rev.*, **89E**, 023007, https://doi.org/10.1103/PhysRevE.89.023007.

Lan, C., H. Liu, D. Li, G. Katul, and D. Finn, 2018: Distinct turbulence structure in stably stratified boundary layers with weak and strong surface shear. *J. Geophys. Res. Atmos.*, **123**, 7839–7854, https://doi.org/10.1029/2018JD028628.

Luhar, A. K., P. J. Hurley, and K. N. Rayner, 2009: Modelling near-surface low winds over land under stable conditions: Sensitivity tests, flux-gradient relationships, and stability parameters. *Bound.-Layer Meteor.*, **130**, 249–274, https://doi.org/10.1007/s10546-008-9341-7.

Mahrt, L., 2011: The near-calm stable boundary layer. *Bound.-Layer Meteor.*, **140**, 343–360, https://doi.org/10.1007/s10546-011-9616-2.

——, and N. Gamage, 1987: Observations of turbulence in stratified flow. *J. Atmos. Sci.*, **44**, 1106–1121, https://doi.org/10.1175/1520-0469(1987)044<1106:OOTISF>2.0.CO;2.

——, and D. Vickers, 2006: Extremely weak mixing in stable conditions. *Bound.-Layer Meteor.*, **119**, 19–39, https://doi.org/10.1007/s10546-005-9017-5.

——, J. Sun, W. Blumen, T. Delany, and S. Oncley, 1998: Nocturnal boundary layer regimes. *Bound.-Layer Meteor.*, **88**, 255–278, https://doi.org/10.1023/A:1001171313493.

——, S. Richardson, N. Seaman, and D. Stauffer, 2012: Turbulence in the nocturnal boundary layer with light and variable winds. *Quart. J. Roy. Meteor. Soc.*, **138**, 1430–1439, https://doi.org/10.1002/qj.1884.

——, C. Thomas, S. Richardson, N. Seaman, D. Stauffer, and M. Zeeman, 2013: Non-stationarity generation of weak turbulence for very stable and weak-wind conditions. *Bound.-Layer Meteor.*, **147**, 179–199, https://doi.org/10.1007/s10546-012-9782-x.

Malhi, Y. S., 1995: The significance of the dual solutions for heat fluxes measured by the temperature fluctuation method in stable conditions. *Bound.-Layer Meteor.*, **74**, 389–396, https://doi.org/10.1007/BF00712379.

Mellor, G. L., and T. Yamada, 1982: Development of a turbulence closure model for geophysical fluid problems. *Rev. Geophys.*, **20**, 851–875, https://doi.org/10.1029/RG020i004p00851.

Monahan, A. H., T. Rees, Y. P. He, and N. McFarlane, 2015: Multiple regimes of wind, stratification, and turbulence in the stable boundary layer. *J. Atmos. Sci.*, **72**, 3178–3198, https://doi.org/10.1175/JAS-D-14-0311.1.

Mortarini, L., E. Ferrero, S. Falabino, S. Trini Castelli, R. Richiardone, and D. Anfossi, 2013: Low-frequency processes and turbulence structure in a perturbed boundary layer. *Quart. J. Roy. Meteor. Soc.*, **139**, 1059–1072, https://doi.org/10.1002/qj.2015.

——, S. Maldaner, L. Moor, M. Stefanello, O. Acevedo, G. Degrazia, and D. Anfossi, 2016a: Temperature autocorrelation and spectra functions in low-wind meandering conditions. *Quart. J. Roy. Meteor. Soc.*, **142**, 1881–1889, https://doi.org/10.1002/qj.2796.

——, M. Stefanello, G. Degrazia, D. Roberti, S. Trini Castelli, and D. Anfossi, 2016b: Characterization of wind meandering in low-wind-speed conditions. *Bound.-Layer Meteor.*, **161**, 165–182, https://doi.org/10.1007/s10546-016-0165-6.

——, D. Cava, U. Giostra, O. Acevedo, L. Nogueira Martins, P. E. Soares de Oliveira, and D. Anfossi, 2018: Observations of submeso motions and intermittent turbulent mixing across a low level jet with a 132-m tower. *Quart. J. Roy. Meteor. Soc.*, **144**, 172–183, https://doi.org/10.1002/qj.3192.

Pahlow, M., M. B. Parlange, and F. Porté-Agel, 2001: On Monin–Obukhov similarity in the stable atmospheric boundary layer. *Bound.-Layer Meteor.*, **99**, 225–248, https://doi.org/10.1023/A:1018909000098.

Pope, S. B., 2000: *Turbulent Flows*. Cambridge University Press, 771 pp.

Poulos, G. S., and Coauthors, 2002: CASES-99: A comprehensive investigation of the stable nocturnal boundary layer. *Bull. Amer. Meteor. Soc.*, **83**, 555–581, https://doi.org/10.1175/1520-0477(2002)083<0555:CACIOT>2.3.CO;2.

R Core Team, 2017: R: A language and environment for statistical computing. R Foundation for Statistical Computing, https://www.R-project.org/.

Sharan, M., M. Modani, and A. Yadav, 2003: Atmospheric dispersion: An overview of mathematical modeling framework. *Proc. Indian Natl. Sci. Acad.*, **69A**, 725–744.

Sorbjan, Z., and A. A. Grachev, 2010: An evaluation of the flux–gradient relationship in the stable boundary layer. *Bound.-Layer Meteor.*, **135**, 385–405, https://doi.org/10.1007/s10546-010-9482-3.

Stull, R. B., 1988: *An Introduction to Boundary Layer Meteorology*. Kluwer Academic, 666 pp.

Sun, J., L. Mahrt, R. M. Banta, and Y. L. Pichugina, 2012: Turbulence regimes and turbulence intermittency in the stable boundary layer during CASES-99. *J. Atmos. Sci.*, **69**, 338–351, https://doi.org/10.1175/JAS-D-11-082.1.

van de Wiel, B. J. H., R. Ronda, and H. J. J. Jonker, 2012a: The cessation of continuous turbulence as precursor of the very stable nocturnal boundary layer. *J. Atmos. Sci.*, **69**, 3097–3115, https://doi.org/10.1175/JAS-D-12-064.1.

——, ——, ——, P. Baas, S. Basu, J. M. M. Donda, J. Sun, and A. A. M. Holtslag, 2012b: The minimum wind speed for sustainable turbulence in the nocturnal boundary layer. *J. Atmos. Sci.*, **69**, 3116–3127, https://doi.org/10.1175/JAS-D-12-0107.1.

Vickers, D., and L . Mahrt, 2006: A solution for flux contamination by mesoscale motions with very weak turbulence. *Bound.-Layer Meteor.*, **118**, 431–447, https://doi.org/10.1007/s10546-005-9003-y.

Zilitinkevich, S. S., T. Elperin, N. Kleeorin, and I. Rogachevskii, 2007: Energy and flux-budget (EFB) turbulence closure model for stably stratified flows. Part I: Steady-state, homogeneous regimes. *Bound.-Layer Meteor.*, **125**, 167–191, https://doi.org/10.1007/s10546-007-9189-2.